Simultaneous Synthesis of One-and Two-Dimensional Gold Nanostructures/Reduced Graphene Oxide Composites in the Redox-Active Ionic Liquid/Water Interfacial System

AUTHOR(S):

Zhang, Yu; Nishi, Naoya; Koya, Ippei; Sakka, Tetsuo

Simultaneous Synthesis of One-and Two-dimensional Gold Nanostructures/Reduced Graphene Oxide Composites in the Redox-active Ionic Liquid/Water Interfacial System

Yu Zhang [a], Naoya Nishi[a], Ippei Koya[a], and Tetsuo Sakka[a]*

[a] Y. Zhang, N. Nishi, I. Koya, and T. Sakka

Department of Energy and Hydrocarbon Chemistry, Graduate School of Engineering, Kyoto University.

Kyoto 615-8510, Japan.

E-mail: nishi.naoya.7e@kyoto-u.ac.jp

Abstract

In this study, one- and two-dimensional (1D and 2D) Au nanostructure/reduced graphene oxide (rGO) composites are simultaneously prepared via a redox-active ionic liquid (RAIL)|water (W) interfacial method without the use of a capping agent. The RAIL (ferrocenylmethyl)dodecyldimethylammonium tetrakis[3,5-bis(trifluoromethyl)phenyl]borate ([FcMDDA$^+$][TFPB$^-$]) plays the dual role of a hydrophobic liquid supporting the interfacial system as well as a reducing agent for the metal precursor and graphene oxide (GO). The RAIL|W interfacial system provides two kinds of composites in the growth regions with no interference between them, namely, Au nanofiber/rGO composites at the RAIL|W interface and Au nanosheet/rGO composites in the bulk of W, which can be easily separated after synthesis. The spontaneous formation mechanism of the two Au-rGO composites has been discussed in detail. Thus, an efficient strategy to prepare 1D and 2D Au-rGO composites simultaneously is developed by employing an interfacial system, which provides a new direction in the synthesis of metal–GO composites.

Introduction

Au nanostructures, with a variety of morphologies, have at least one dimension that is limited to a nanoscale. They have received considerable attention from researchers owing to the fascinating chemical and physical properties that bulk Au does not exhibit. Among them, a series of one-or two-dimensional (1D or 2D) Au nanostructures, including nanowires [1, 2], nanofibers (NFs) [3], nanobelts [4], nanosheets (NSs) [5], and nanoplates [6], have shown extraordinary application performance in the fields of electronics [7], photonics [8], catalysis [9], and sensing [10–14]. From previous studies, it has been widely recognized that the properties of Au nanostructures are highly associated with the size, shape, morphology, and dimensionality [15, 16]. 1D or 2D Au nanostructures exhibit some unique properties owing to their distinctive morphologies, which can be specifically applied in different application fields [17, 18].

Recently, the introduction of Au nanostructures on graphene-based derivatives to form composites has attracted significant interest of researchers [19–22]. Graphene is a one-atom-thick, 2D planar material with a sp^2-bonded carbon structure, showing fascinating properties such as high specific surface area, high mechanical strength, and excellent electrical conductivity. GO, which can be produced by the chemical oxidation of graphite, possesses good dispersibility in water because of the presence of oxygen-containing functional groups. This property of GO is beneficial to prepare GO-based composites by wet-chemical methods [23–25]. Graphene derivatives in such composites not only support the nanostructures for preventing aggregation, but also, more importantly, improve their application performance resulting from its unique properties. For example, graphene derivatives can facilitate the adsorption of some molecules via π–π stacking or hydrophobic interactions [26]. The electrical conductivity of composites can be greatly improved after GO is reduced to rGO [27]. Moreover, studies revealed that GO contributes to improving surface-

enhanced Raman spectroscopy (SERS) activity through chemical enhancement for Au–GO composites [28, 29]. To date, there are several strategies to produce anisotropic Au nanostructures on graphene derivatives [20, 30, 31–38]. Xiao *et al.* reported an in situ synthesis of ultrathin Au nanowires (NWs) on GO sheets by using 1-amino-9-octadecene adsorbed on the GO surface as the reducing agent for $AuCl_4^-$ as well as the 1D structure-directing agent [20]. Zhang *et al.* fabricated Au nanoplate/GO composites using tannic acid as the reducing agent for Au precursor and the immobilizing agent on GO surfaces [30]. Owing to the shape-dependent properties of anisotropic Au nanostructures [39, 40], the specific synthesis of 1D or 2D Au nanostructures on graphene derivatives is useful in different application fields. However, most of the synthesis strategies proceed in one-phase systems, restricting Au nanostructures to form only one shape owing to the homogenous environment. A strategy that can simultaneously prepare 1D and 2D Au nanostructures on graphene derivatives and easily separate them after the synthesis would be efficient and productive, which will decrease the time, source, and energy consumption during the synthesis. To the best of our knowledge, there is no reported method that can produce 1D and 2D Au nanostructures on graphene derivatives simultaneously.

The liquid–liquid (L–L) interface between oil (O) and water (W) has been applied as the formation site for the synthesis of noble metal nanoparticles in the past [41–51]. Rao *et al.* prepared a broad range of nanostructures made of materials, including metals, chalcogenides, and oxides, at the toluene–water interface [45–48], thereby, verifying the wide practicability of the L–L interfacial strategy in the field of nanomaterial synthesis. This interfacial method separates the metal precursor from the reducing agent by dissolving them into different liquid phases, thus confining the redox reaction to occur spatial-selectively only at the interface. Moreover, the formed metal nanoparticles at the L–L interface can also be the redox catalyst, facilitating heterogeneous electron transfer (ET) reactions between two liquid phases [52–54]. Traditional organic solvents in the

O|W interfacial method can be replaced with ionic liquids (ILs), which are liquid salts entirely composed of cations and anions. The IL|W interfacial method has been investigated to prepare metal nanostructures [55–58]. The introduction of an IL endows the interfacial method with controllability, since the chemical and physical properties of ILs are adjustable by elaborate designs of the chemical structures of cations and anions. Except for just as a hydrophobic solvent, ILs can actively play multiple roles in the IL|W interfacial system. For instance, the high viscosity of an IL as well as the interfacial structure formed by IL ions could induce the anisotropic growth of 1D nanostructures. We have successfully prepared 1D nanostructures of Au [59, 60], Pt [61], Pd [62], and Au–Pd bimetal [63] by employing the IL|W interface method in our previous studies. The metal nanostructures formed at the IL|W interface are prevented from agglomeration, which is possibly due to the rigid multilayering structures formed by IL ions at the interface [64]. Moreover, the IL|W interfacial system provides two disparate growth environments towards W and IL for metal nanostructures and makes it possible to connect the two portions with different morphologies together with the joint at the IL|W interface [61]. When an IL contains a redox-active group with cations or anions, such as RAIL, it can act as a reducing agent for metal precursor and liquid substrate simultaneously in the RAIL|W interfacial system. Our previous studies manifested that the RAIL|W interfacial system can be used for the synthesis of metal nanostructures and play an indispensable role for the growth of metal nanostructures [62, 63].

In the present work, we introduce a facile method to prepare 1D and 2D Au nanostructures/rGO composites in the RAIL|W interfacial system simultaneously without the use of a capping agent or a surfactant. The RAIL (ferrocenylmethyl)dodecyldimethylammonium tetrakis[3,5-bis(trifluoromethyl)phenyl]borate ([$FcMDDA^+$][$TFPB^-$]) [65, 66] not only plays the role of a reducing agent but also supports the interfacial system as the liquid substrate, and its high viscosity is also crucial for inducing 1D Au nanostructures.

The RAIL|W interfacial system provides two formation regions: i) the RAIL|W interface for Au nanofiber/rGO (Au NF/rGO) composites, and ii) the bulk of W for Au nanosheet/rGO (Au NS/rGO) composites. The two composites can be easily separated from each other after the synthesis. GO plays crucial roles in realizing the reduction of Au precursor and the formation of Au NS in W. The possible formation mechanisms for Au NF/rGO and Au NS/rGO are investigated in detail. Our study provides a new strategy for the simple and simultaneous synthesis of Au 1D and 2D nanostructure/rGO composites in one system.

Experimental

1. Synthesis of the RAIL [FcMDDA$^+$][TFPB$^-$]

The synthesis of [FcMDDA$^+$][TFPB$^-$] follows the same method in our previous report [63].

2. Preparation of GO dispersed solution

GO was prepared by modified Hummers' method [67]. Graphite powder (2 g, Fujifilm Wako Pure Chemical Corporation, Wako Special Grade) and $NaNO_3$ (1.8 g) were introduced into ice-cooled concentrated H_2SO_4 (98%, 50 mL). $KMnO_4$ (6 g) was slowly added to the solution while it was stirred; the solution was stirred at 35 °C for 30 min. 100 mL of deionized water was added to dilute the solution that induced the temperature to increase rapidly to 98 °C, and the system was maintained at this temperature for 15 min. Finally, the reaction was terminated by adding H_2O_2 (3 wt% aqueous solution, 20 mL) dropwise while stirring the solution at room temperature until the suspension turned bright yellow. The obtained product was first washed by a 5% HCl solution, and then 50 mL of deionized water was added, followed by centrifuging at 3000 rpm. The resulting supernatant was collected and was repeatedly washed by deionized water with a centrifugation of 12000 rpm, until pH of the liquid approached 7. The prepared GO was dried in vacuum and dispersed in deionized water of 5

mg/mL by an ultrasonic bath.

3. The simultaneous synthesis of Au NF/rGO and NS/rGO composites

The simultaneous synthesis of Au NF/rGO and NS/rGO composites was realized by the following procedures: i) 20 μL of GO dispersed water (5 mg/mL) was added to 2 mL of 10 mM $HAuCl_4$ (0.1 M HCl aqueous solution) and then treated with an ultrasonic bath for 10 min in order to sufficiently mix the two components, and ii) The GO-dispersed solution was gently pipetted onto 0.2 g of RAIL $[FcMDDA^+][TFPB^-]$ in a 3 mL glass bottle, and then the L–L two-phase system was kept at 70 °C for 24 h in a thermostatic bath without disturbing the solution. In the present system, a static reaction environment was particularly crucial for obtaining the uniform growth of the Au nanostructures. After the 24 h reaction, an immobile black deposit layer was found at the RAIL|W interface. Meanwhile, some flocculent precipitates in W were found that had piled upon the RAIL|W interface, which was easily collected by pipetting the W that was followed by centrifugation. After W was removed, the black deposit at the RAIL surface was collected by adding the mixed solvent (50:50 vol%) of methanol and dichloromethane (DCM) to dissolve the RAIL that was followed by centrifugation. The obtained two precipitates were washed more than ten times by methanol and DCM and was conserved separately.

4. Characterization of materials

The prepared Au NF/rGO and Au NS/rGO composites were suspended in DCM, dropped onto an Al foil and a copper grid, and observed using a scanning electron microscope (SEM) (SU8220, HITACHI) that was equipped with energy dispersive X-ray spectrometer (EDX) and a transmission electron microscope (TEM) (JEM-2100F, JEOL), respectively. X-ray diffraction (XRD) measurements were performed using a RINT-2500 (RIGAKU) equipped with a

Cu Kα source (40 kV, 200 mA, λ = 0.154 nm). The Fourier transform infrared spectroscopy (FTIR) (Infinity Gold MI Plus, Thermo Mattson) measurements were carried out by dispersing samples in potassium bromide pellets.

Results and discussion

Fig. 1(a) shows the photos of the L–L two-phase system before and after 10 min, 1 h, and 24 h reactions, respectively. Before the reaction, GO was uniformly dispersed in W. After 10 mins, brown flocculent precipitates were observed in W, and a black deposit layer was found at the RAIL|W interface. After 1 h, the precipitates in W gradually sank and finally piled upon the RAIL|W interface after the 24 h reaction. Moreover, the color of the RAIL gradually became black during the reaction because of the oxidation of $FcMDDA^{+}$ to $FcMDDA^{2+}$, implying that the RAIL was actively involved in the interfacial ET reaction, rather than remaining a liquid substrate to form an interface with W. The brown flocculent precipitates found in W after 10 min should be the aggregated GO. The acidic environment of W (0.1 M HCl) hindered the ionization of carboxylic groups in GO and thereby induced its aggregation [68]. Several studies reported that GO can be self-assembled at the O|W interface owing to its amphiphilic property [69–71]. In the present study using an acidic solution, the hydrophobicity of GO is enhanced due to the low ionization of the carboxylic groups, which not only promoted the adsorption of GO near the RAIL|W interface at the interface, but also facilitated the aggregation of GO far away from the interface in bulk W (t = 10 min as shown in Fig. 1(a)). As can be observed in the photographs from t = 10 min to 24 h (Fig. 1(a)), the aggregated GO gradually sinks owing to gravity and finally piles upon the RAIL|W interface. Two kinds of precipitates can be observed in the system after the 24 h reaction (Fig. 1(a)); one is piled upon the RAIL|W interface in W, and the other is the black layer deposited at RAIL|W interface. They were separately collected and investigated

using SEM and EDX measurements. For the precipitates in W that are piled upon the RAIL|W interface (Fig. 1(b)), it can be observed that many triangular and hexagonal Au NSs (marked with the green arrow) are uniformly distributed on rGO layers (marked with the white arrow, the formation of rGO will be proved later), with thicknesses of approximately 60 nm (Fig. S1) and widths of several micrometers. The Au NSs in the present study are significantly wider than those with sub-micrometer widths in Au–graphene derivative composites that were reported previously [30, 33, 36, 37]. For the precipitate deposited at the RAIL|W interface (Fig. 1(c)), it can be observed that a large amount of Au NFs (marked with the red arrow) are immobilized on the surface of the rGO (marked with the white arrow; the formation of rGO will be proved later). The formed Au NFs are highly flexible with a uniform diameter of approximately 50~100 nm and a length of several tens of micrometers; they are similar to the ones synthesized at the IL|W interface [59] and the RAIL|W interface [63] in our previous studies without using GO. The EDX mappings for the two composites are shown in Fig. 1(d) and Fig. 1(e). The element distributions of Au and carbon are identical with their morphology in the corresponding SEM images, demonstrating the successful formation of Au-rGO composites.

XRD analysis was performed to further identify the phase of the prepared composites and the results are shown in Fig. 2(a). GO shows a typical diffraction peak at 2θ = 9.96°, which corresponds to (111) plane of GO, confirming the successful preparation of GO. The XRD patterns of the prepared composites of Au NF/rGO and Au NS/rGO exhibit typical diffraction peaks of Au, demonstrating the successful reduction of Au. The peak at 9.96° thoroughly disappeared due to the disruption of the regular layer structures of GO by deposition of Au on the rGO surface. It is noted that the diffraction peak at 2θ = 38.2° for the Au NS/rGO composite is considerably stronger than that of the others; this indicates that Au NS has a preferred orientation of (111) surface along the XRD substrate and implies that the triangular and hexagonal surface

of Au NS is Au (111) plane. Fig. 2(b) shows a TEM image for the Au NS/rGO composites, where the hexagonal morphology of Au NS on a large piece of GO layer with wrinkles can be clearly discerned. The corresponding selected area electron diffraction (SAED) pattern (Fig. 2(b), inset) presents a hexagonal symmetry and a single-crystalline feature, reflecting the hexagonal arrangement of Au atoms along the (111) surface. The above results confirmed the single-crystalline structure for the Au NS composited with rGO.

The fact that Au NF/rGO composites were collected from the RAIL|W interface revealed their formation sites. In a previous study, we had successfully prepared Janus-type Au/polythiophene composites by applying the IL|W interfacial method [60]. In the present study, Au NF/rGO composites were formed by taking the RAIL|W interface as a confined self-assembly region, where GO was spontaneously adsorbed on the RAIL|W interface, and $AuCl_4^-$ was spontaneously reduced to form Au NFs on the RAIL side of the RAIL|W interface. In our previous research [63], we had measured the standard redox potential of the reducing agent $FcMDDA^+$, which was approximately −0.14 V *vs.* SHE (standard hydrogen electrode) in acetonitrile containing 0.1 M tetraethylammonium perchlorate at 298 K. It was much lower than the standard redox potential of $AuCl_4^-$ (+1.00 *vs.* SHE [73]) and that of GO (+0.38 *vs.* SHE [74]), indicating that $FcMDDA^+$ has the ability to reduce $AuCl_4^-$ and GO. However, whether an interfacial ET reaction take place not only depends on their redox potential, but also relies on the existence of an ion transfer (IT) reaction that can be coupled with the ET reaction. Since the metal precursor and the reducing agent in IL and W were dissolved separately, the ET reaction across the interface will generate excess negative charges for W and positive charges for IL. Thus, the interfacial ET cannot take place individually, unless it was coupled with another charge transfer reaction (for instance, the IT of the anion from W to IL or the IT of the cation from RAIL to W) to neutralize the excess charges brought by ET [59–63]. Previous studies confirmed that $AuCl_4^-$, as a moderately

hydrophobic species, could be easily transferred across the O|W [75] and IL|W [59, 60, 63] interfaces within the potential window. In our study, we used the same RAIL|W interfacial system [63], and it was demonstrated that the IT of $AuCl_4^-$ (Equation 1) from W to RAIL was coupled with the ET between $AuCl_4^-$ and the redox-active cation $FcMDDA^+$ (Equation 2) [63], which led to the total interfacial reaction (Equation 3).

$$AuCl_4^- (W) \rightarrow AuCl_4^- (RAIL) \quad (1)$$

$$3FcMDDA^+ (RAIL) + AuCl_4^- (W) \rightarrow 3FcMDDA^{2+} (RAIL) + Au + 4Cl^- (W) \quad (2)$$

$$3FcMDDA^+ (RAIL) + 4AuCl_4^- (W) \rightarrow 3FcMDDA^{2+} (RAIL) + Au + 4Cl^- (W) + 3AuCl_4^- (RAIL) \quad (3)$$

Similarly, the above interfacial reactions occurred in the present system, which enabled the occurrence of the spontaneous reduction of $AuCl_4^-$ at the RAIL|W interface. The IT of $AuCl_4^-$ from W to IL (Equation 1) was driven by the ET between the reducing agent in IL and $AuCl_4^-$ in W (Equation 2), the latter released four hydrophilic Cl^- ions towards W. This liberation of hydrophilic Cl^- to W was a big driving force for the interfacial ET reaction. For the spontaneous formation of Au NF/rGO composites at the RAIL|W interface, the adsorption of GO and the IT and ET of $AuCl_4^-$ had taken place at the interface simultaneously, which led to the formation of Au NF/rGO composites. Since $AuCl_4^-$ and GO could directly contact the reducing agent $FcMDDA^+$ at the RAIL|W interface, $AuCl_4^-$ (+1.00 *vs*. SHE [73]) was likely to be reduced earlier than GO (+0.38 *vs*. SHE [74]) due to its more positive standard redox potential.

In our previous study [72], the IL was replaced with 1,2-dichloroethane (DCE) in the interfacial system to determine the effect of the IL on the morphology of the formed Au nanostructures. We also examined a thickened

DCE by adding a polymer, which functioned as a thickener, to the DCE. The morphology of Au nanostructures changed from irregular particles for the neat DCE to 1D NFs for the thickened DCE. However, even when an amount of IL was added to DCE with a marginal viscosity change, morphology change was still observed. These experiments manifested that the high viscosity of IL as well as the interfacial structure formed by IL ions contributed to inducing the anisotropic growth of 1D metal nanostructures. This conclusion was repeatedly confirmed in our subsequent studies [59–63], which explains the formation of Au NFs in the present case. A control experiment was performed to further confirm the idea. The RAIL phase was diluted with DCE (2 mL) so that its viscosity was greatly lowered, and the interfacial system reacted with the other conditions remained unchanged. According to the corresponding SEM images for the obtained product in the system (Fig. S2), Au in the composites, collected in W, is the morphology of NS (Fig. S2(a)), thereby indicating that the formation of NS morphology in W is irrelevant to the state of RAIL phase. However, Au dendrites rather than Au NFs are obtained for the composites collected at the DCE(RAIL)|W interface (Fig. S2(b)). This clearly verified that the 1D morphology of Au NF resulted from the use of RAIL rather than GO.

According to Fig. 1(b) and Fig. 1(d), the black precipitates collected in Ware Au NS/rGO composites. However, it is difficult to understand how $AuCl_4^-$ is reduced in W, because the only reducing agent $FcMDDA^+$ (the redox-active cation of RAIL) is separated from W in the present interfacial system. Two control experiments were performed to explain the above question. In the first case, W used in the synthesis of GO and $AuCl_4^-$ reacted at 70 °C without RAIL. UV–vis spectra for W and the photos of the system before and after 24 h reaction are shown in Fig. 2(c). Before the reaction (t = 0), the UV–vis spectrum of the W manifests an overlapped absorption of GO and $AuCl_4^-$ (red), corresponding to the photo (t = 0), showing that GO is uniformly mixed with $AuCl_4^-$ in W. After the 24 h reaction, it is (t = 24 h) clearly seen that GO is aggregated and sinks to

the bottom of the bottle owing to the acidic condition. The corresponding UV spectrum of the W (t = 24 h, supernatant) manifests only $AuCl_4^-$ adsorption peak at 313 nm with a basically unchanged intensity (blue, the slight decrease is due to the removal of GO absorption because of the aggregation). The following two conclusions can be obtained from the above control experiment: (i) $AuCl_4^-$ cannot be reduced by GO, and (ii) the reduction of $AuCl_4^-$ in W related to the use of RAIL. In the second case, GO was dispersed in 0.1 M HCl or deionized water in the absence of $AuCl_4^-$ that was applied as W to form the interface with RAIL, and the systems were reacted at 70 °C for 24 h. The photos of the two systems before and after the reactions are shown in Fig. S3. When only GO is dispersed in 0.1 M HCl (Fig. S3A) in the absence of $AuCl_4^-$, it can be clearly observed that GO in W aggregated and contacted the RAIL|W interface through linkage with each other after the 24 h reaction. However, when GO is dispersed in deionized water (Fig. S3B), GO remains in the dispersed state in W after 24 h, verifying that the aggregation of GO is due to the acidic condition of W. UV–vis measurements were performed for the W containing 0.1 M HCl in the RAIL|W interfacial system after the 24 h reaction (Fig. S4) in the presence (blue, the W in Fig. S3A after reaction) or absence of GO (green). A peak at 627 nm arises for the W with the presence of GO (blue), which is attributable to the oxidized cation $FcMDDA^{2+}$ transferred from RAIL to W [62, 63]. However, this peak cannot be found for W without GO (green). The above results imply that $FcMDDA^{2+}$ was generated by the ET reaction between GO and the reducing agent $FcMDDA^+$, and some $FcMDDA^{2+}$ was transferred from RAIL to W, in order to balance the excess charges brought by ET. This is in contrast to the condition where both $AuCl_4^-$ and GO were added in W, and IT of $AuCl_4^-$ occurred instead of $FcMDDA^{2+}$. This can be explained thermodynamically. The IT of $AuCl_4^-$ from W to RAIL was more favored to take place and coupled with the ET compared to the IT of $FcMDDA^{2+}$ from RAIL to W, owing to the more positive formal potential (see SI for details). For the case where GO was added to W without

$AuCl_4^-$, there remained only one candidate for IT reaction, which was the IT of $FcMDDA^{2+}$ from RAIL to W. The above control experiment implies that GO can be reduced by RAIL in the RAIL|W interfacial system. In order to verify this conclusion, FTIR measurements were performed for GO, rGO reduced by RAIL (RAIL-rGO, collected from the system in Fig. S3A), and rGO reduced by L-Ascorbic acid (L-rGO) as a comparison, and the results are shown in Fig. 2(d). The RAIL-rGO shows similar absorption with L-rGO, where the intensities of the absorption peaks related to C=O (1720 cm^{-1}), C–O–H (1388 cm^{-1}), and C–O (1180 and 1095 cm^{-1}) stretching are apparently decreased compared to GO [76, 77], indicating the successful reduction of GO to rGO using RAIL as the reducing agent in the RAIL|W interfacial system. It should be noted that only a small amount of GO could directly contact the reducing agent $FcMDDA^+$ by adsorbing at the RAIL|W interface; the redundant GO in W was aggregated and piled on the RAIL|W interface as shown in Fig. S3A. However, FTIR results demonstrated that all of GO, including the aggregated GO in W, was reduced to rGO, implying that the reduction of GO in W may not require the actual contact with the reducing agent $FcMDDA^+$, but the reduction could happen through an indirect contact mode. GO adsorbed at the RAIL|W interface will be reduced first due to the direct contact with the reducing agent, and transform to rGO film with good electron conductivity fully covering the RAIL|W interface. The GO in W can be reduced through rGO delivering electrons from RAIL to W. The above situation can be extended to the present synthesis condition for Au-GO composites. The acidic condition of W facilitates GO to be aggregated, followed by being reduced to rGO to form an electron conduction route to deliver electrons, and then $AuCl_4^-$ can be reduced by the delivered electron on the rGO surface.

The above discussion explained how $AuCl_4^-$ was reduced in W; however, the reason for obtaining 2D Au NSs instead of other morphologies is not clear. In most reported studies [78–80], the formation of Au NSs involved the use of capping agents (such as poly (vinylpyrrolidone) or

hexadecyltrimethylammonium bromide) to selectively adsorb the specific facet of Au, thereby inducing an anisotropic growth of Au toward 2D nanostructures. In the present study, no species in W, which only contains H^+, $AuCl_4^-$, Cl^-, and GO, could play the role of a capping agent. Considering the 2D planar characteristic of GO, the formation of Au 2D nanostructures was likely to be templated by GO. According to some references, Au NS/GO composites were prepared by immobilization of the Au precursor or the reducing agent on the GO surface [30–36] so that Au could grow toward 2D nanostructures by taking GO as the template. In these cases, through anchoring one of the reaction species on the GO planes, the free growth of Au in the directions other than along the GO plane was prevented, so that GO could play the role of the template to induce the 2D growth of Au. Therefore, we assumed that the limit of the reduction sites of $AuCl_4^-$ on the GO surface was the key factor to activate the 2D template function of GO (we further discuss the mechanism in the following paragraph). A control experiment was performed to verify the aforementioned assumption. Methanol (10 mL) was added to the typical synthesis system to remove the interface, and the obtained one-phase mixture reacted at 70 ºC, when it was stirred. The SEM image and schematic for Au-rGO composites obtained in the one-phase system is shown in Fig. 3 (upper panel). Although large amount of GO still exists in the one-phase mixture and can play the role of the 2D template, only Au particles can be found on the GO surfaces. In this case, the limited growth of Au along the GO plane was eliminated by the free contact of the two redox species ($AuCl_4^-$ and $FcMDDA^+$) in the one-phase mixture. The irregular morphology of Au nanostructures might be formed first in the one-phase mixture, and then attached to the GO surface. However, in the case of the formation of Au NS by using the RAIL|W interfacial system (Fig. 3, lower), owing to the lack of a reducing agent in W, the reduction of $AuCl_4^-$ is only limited on the rGO plane, through rGO delivering electrons from RAIL to W. The acidic condition of W facilitated small GO flakes to aggregate and form a larger piece. According to Fig. 1(b), although

the lateral size of Au NS has reached several micrometers, it can be clearly observed that the rGO underneath Au NS is considerably larger than Au NS. The control experiment demonstrated that rGO plays the role of the 2D template by restricting the reduction sites of $AuCl_4^-$ on the GO surface. We checked whether the acidic environment was related to the formation of 2D Au NSs in the present study. We added 0.1 M LiCl instead of 0.1 M HCl to W to form a neutral environment, and the other conditions remained unchanged. The high concentration of the electrolyte LiCl (0.1 M) could still induce the aggregation of GO in W owing to the weak electrostatic repulsion (short Debye length) [81], so that $AuCl_4^-$ in W could be reduced on the rGO surface because of similar reasons that have been discussed in the case of the acidic condition. The corresponding SEM images of the obtained product are shown in Fig. S5. It can be clearly observed that Au shows the same morphology of NS and NF in the two composites that were collected in W and at the RAIL|W interface, respectively, thereby indicating that the formation of Au NS was independent of the acidic environment.

The SEM images of Au NS/rGO composites with a high resolution displaying the details of Au NSs are shown in Fig. S6. In Fig. S6(a), it is seen that Au NSs are overlapped, and the wrinkles of rGO can also be distinctly observed on the Au surface. Moreover, according to Fig. S6(b) and Fig. 6(c), it can be clearly discerned that all Au NSs are wrapped by some transparent films. EDX mappings in Fig. S7 show the element distributions for Au and carbon. They are identical to the corresponding morphology of Au NSs and the typical wrinkles of rGO, respectively, confirming that these transparent films are rGO. The above results manifest that the Au NS/rGO composites possess piled nanostructures with multiple layers of rGO, where Au NSs are inserted between rGO layers, as shown schematically in Fig. S6(d). Such unusual piled nanostructures are caused by the two situations, namely, rGO is piled either before or after the formation period of Au. The former situation is more

reasonable for our case, since GO was found to be aggregated only after 10 min of the reaction (Fig. 1(a)), and was followed by reduction to rGO. Liang *et al.* prepared 2D Au nanostructures by using layered double hydroxides (LDHs) with lamellar structures as the 2D template. In this method, Au precursors ($AuCl_4^-$) were introduced into the interlayer space of Mg/Al LDH due to the anion-exchange capability of LDH, thereby confining the 2D Au NSs formed between the metal hydroxide layers of LDH after the chemical reduction [82]. In the present case, considering that aggregated rGO also had lamellar structures with similar 2D planar characteristic, we can infer that the formation of such multi-piled Au NS/rGO nanostructures is realized by the intercalation and reduction of $AuCl_4^-$ between the rGO layers. The overlap of Au NSs observed in Fig. S6(a) is due to the multi-piled nanostructures of composites, where Au NSs are sandwiched between the rGO layers.

The possible mechanism for the simultaneous formation of 1D and 2D Au nanostructures/rGO composites in the RAIL|W interfacial system is illustrated in Fig. 4. Initially, GO flakes were uniformly dispersed in W (Fig. 4(a)). As the reaction proceeded, GO flakes were spontaneously adsorbed at the RAIL|W interface followed by being reduced as rGO films, whereas the redundant GO flakes in W were aggregated and gradually piled upon the RAIL|W interface. The IT of $AuCl_4^-$ from W to RAIL, which took place throughout the reaction, was coupled with the ET for the reduction of $AuCl_4^-$ (Fig. 4(b)). After making contact with the RAIL|W interface, which was already covered by rGO films, the aggregated GO in W was reduced by the electrons delivered from $FcMDDA^+$ in RAIL through the rGO film. The rGO became the electron media, enabling the reduction of $AuCl_4^-$ between the multilayers (Fig. 4(c)). Finally, Au NSs were formed by taking rGO as the 2D template, while the high viscosity of RAIL as well as the interfacial structure formed by IL-ions induced Au NFs that were formed on the RAIL side of the RAIL|W interface (Fig. 3(d)). The spontaneous formation of Au NF/rGO and Au NS/rGO composites simultaneously was

realized in the RAIL|W interfacial system.

Conclusions

We prepared two composites of Au NF/rGO and Au NS/rGO in one RAIL|W interfacial system simultaneously, where the use of the capping agent or surfactant was not required. The RAIL [FcMDDA$^+$][TFPB$^-$] was the reducing agent for both $AuCl_4^-$ and GO. Au NS/rGO and Au NF/rGO composites were formed in bulk W and at the RAIL|W interface of the system, respectively, which could be easily separated from each other after the synthesis. The acidic condition facilitated the GO to be adsorbed at the RAIL|W interface and the redundant GO in W aggregated to establish contact between them. GO adsorbed at the RAIL|W interface was first reduced to rGO with good conductivity, which became the electron transfer media, enabling reduction of the redundantly aggregated GO and the Au precursor in W in the absence of the reducing agent initially. The high viscosity of the RAIL induced the formation of Au NF deposited on rGO at the RAIL|W interface. Au NS/rGO composites were formed in W by taking rGO planes as the reduction sites and 2D templates. Our study provides a new strategy for the efficient and simultaneous synthesis of Au 1D and 2D nanostructure/rGO composites in one system.

Acknowledgements

We acknowledge Dr. Yoji Kobayashi for the TEM and SAED measurements as well as Dr. Yuki Kitazumi for the FTIR measurements. This work was partly supported by JSPS KAKENHI (No. 18K05171), TEPCO Memorial Foundation, and Kato Foundation for Promotion of Science.

Supporting Information

The Supporting Information is available free of charge on the ACS

Publications website at DOI: ***.

SEM images showing the thickness of the Au NS, SEM images of the composites obtained when the RAIL is diluted with an oil, photographs and UV-Vis spectra of W for the RAIL-W two-phase system in the absence of GO and those in the absence of both GO and $AuCl_4$-, SEM images of the composites obtained when HCl is replaced with LiCl, SEM images and EDX mappings showing the piled multilayer structure of Au Ns/rGO composites, and the calculation of the formal potentials from the mid-point potentials for IT reactions (PDF)

Reference

1. Huo, Z.; Tsung, C.-k.; Huang, W.; Zhang, X.; Yang, P. Sub-Two Nanometer Single Crystal Au Nanowires. *Nano lett.* **2008**, *8*, 2041-2044.
2. Wang, C.; Hu, Y.; Lieber, C. M.; Sun, S. Ultrathin Au Nanowires and Their Transport Properties. *J. Am. Chem. Soc.* **2008**, *130*, 8902-8903.
3. Vinod, T. P.; Zarzhitsky, S.; Morag, A.; Zeiri, L.; Levi-Kalisman, Y.; Rapaport, H.; Jelinek, R. Transparent, Conductive, and SERS-Active Au Nanofiber Films Assembled on an Amphiphilic Peptide Template. *Nanoscale* **2013**, *5*, 10487-10493.
4. Chen, Y.; Somsen, C.; Milenkovica, S.; Hassel, A. W. Fabrication of Single Crystalline Gold Nanobelts, *J. Mater. Chem.* **2009**, *19*, 924-927.
5. Li, Z.; Liu, Z.; Zhang, J.; Han, B.; Du, J.; Gao, Y.; Jiang, T. Synthesis of Single-Crystal Gold Nanosheets of Large Size in Ionic Liquids. *J. Phys. Chem. B* **2005**, *109*, 14445-14448.
6. Luo, Y. Large-Scale Preparation of Single-Crystalline Gold Nanoplates. *Mater. Lett.* **2007**, *61*, 1346-1349.
7. Maurer, J. H.; Gonzalez-Garcia, L.; Reiser, B.; Kanelidis, I.; Kraus, T. Templated Self-Assembly of Ultrathin Gold Nanowires by Nanoimprinting

for Transparent Flexible Electronics. *Nano Lett.* **2016**, *16*, 2921-2925.

8. Major, T. A.; Devadas, M. S.; Lo, S. S.; Hartland, G. V. Optical and Dynamical Properties of Chemically Synthesized Gold Nanoplates. *J. Phys. Chem. C* **2013**, *117*, 1447-1452.
9. Chirea, M.; Freitas, A.; Vasile, B. S.; Ghitulica, C.; Pereira, C. M.; Silva, F. Gold Nanowire Networks: Synthesis, Characterization, and Catalytic Activity. *Langmuir* **2011**, *27*, 3906-3913.
10. Gong, S.; Schwalb, W.; Wang, Y.; Chen, Y.; Tang, Y.; Si, J.; Shirinzadeh, B.; Cheng, W. A Wearable and Highly Sensitive Pressure Sensor with Ultrathin Gold Nanowires. *Nat. Commun.* **2014**, *5*, 3132.
11. Feng, H.; Yang, Y.; You, Y.; Li, G.; Guo, J.; Yu, T.; Shen, Z.; Wu, T.; Xing, B. Simple And Rapid Synthesis Of Ultrathin Gold Nanowires, Their Self-Assembly and Application in Surface-Enhanced Raman Scattering. *Chem Commun.* **2009**, *15*, 1984-1986.
12. Liu, H.; Yang, Q. A Two-Step Temperature-Raising Process to Gold Nanoplates With Optical and Surface Enhanced Raman Spectrum Properties. *CrystEngComm.* **2011**, *13*, 2281-2288.
13. Wang, T.; Hu, X.; Wang, J.; Dong, S. Surface-Enhanced Raman Scattering from Surfactant-Free 3D Gold Nanowire Networks Substrates. *Talanta* **2008**, *75*, 455-460.
14. Deckert-Gaudig, T.; Deckert, V. Ultraflat Transparent Gold Nanoplates--Ideal Substrates for Tip-Enhanced Raman Scattering Experiments. *Small* **2009**, *5*, 432-436.
15. Wiley, B.; Sun, Y.; Chen, J.; Cang, H.; Li, Z.-Y.; Li, X.; Xia, Y. Shape-Controlled Synthesis of Silver and Gold Nanostructures. *MRS Bulletin* **2011**, *30*, 356-361.
16. Xiao, J.; Qi, L. Surfactant-Assisted, Shape-Controlled Synthesis of Gold Nanocrystals. *Nanoscale* **2011**, *3*, 1383-1396.
17. Bridges, C. R.; DiCarmine, P. M.; Seferos, D. S. Gold Nanotubes as

Sensitive, Solution-Suspendable Refractive Index Reporters. *Chem. Mater.* **2012**, *24*, 963-965.

18. Andoy, N. M.; Zhou, X.; Choudhary, E.; Shen, H.; Liu, G.; Chen, P. Single-Molecule Catalysis Mapping Quantifies Site-Specific Activity and Uncovers Radial Activity Gradient on Single 2D Nanocrystals. *J. Am. Chem. Soc.* **2013**, *135*, 1845-1852.
19. Tan, C.; Huang, X.; Zhang, H. Synthesis and Applications of Graphene-Based Noble Metal Nanostructures. *Mater. Today* **2013**, *16*, 29-36.
20. Huang, X.; Li, S.; Wu, S.; Huang, Y.; Boey, F.; Gan, C. L.; Zhang, H. Graphene Oxide-Templated Synthesis of Ultrathin or Tadpole-Shaped Au Nanowires with Alternating Hcp and Fcc Domains. *Adv. Mater.* **2012**, *24*, 979-983.
21. Wang, Y.; Polavarapu, L.; Liz-Marzan, L. M. Reduced Graphene Oxide-Supported Gold Nanostars for Improved SERS Sensing and Drug Delivery. *ACS Appl. Mater. Inter.* **2014**, *6*, 21798-21805.
22. Huang, J.; Zhang, L.; Chen, B.; Ji, N.; Chen, F.; Zhang, Y.; Zhang, Z. Nanocomposites of Size-Controlled Gold Nanoparticles and Graphene Oxide: Formation and Applications in SERS and Catalysis. *Nanoscale* **2010**, *2*, 2733-2738.
23. Zhang, H.; Hines, D.; Akins, D. L. Synthesis of a Nanocomposite Composed of Reduced Graphene Oxide and Gold Nanoparticles. *Dalton Trans*. **2014**, *43*, 2670-2675.
24. Dong, X.; Huang, W.; Chen, P. In Situ Synthesis of Reduced Graphene Oxide and Gold Nanocomposites for Nanoelectronics and Biosensing. *Nanoscale Res. Lett.* **2011**, *6*, 60.
25. Li, X.-R.; Li, X.-L.; Xu, M.-C.; Xu, J.-J.; Chen, H.-Y. Gold Nanodendrities on Graphene Oxide Nanosheets for Oxygen Reduction Reaction. J. *Mater. Chem. A* **2014**, *2*, 1697-1703.
26. Nguyen-Phan, T.-D.; Pham, V. H.; Shin, E. W.; Pham, H.-D.; Kim, S.; Chung,

J. S.; Kim, E. J.; Hur, S. H. The Role of Graphene Oxide Content on the Adsorption-Enhanced Photocatalysis of Titanium Dioxide/Graphene Oxide Composites. *Chem. Eng. J.* **2011**, *170*, 226-232.

27. Bao, W.; Zhang, Z.; Qu, Y.; Zhou, C.; Wang, X.; Li, J. Confine Sulfur in Mesoporous Metal–Organic Framework @ Reduced Graphene Oxide for Lithium Sulfur Battery. *J. Alloy Compd.* **2014**, *582*, 334-340.
28. Liu, X.; Cao, L.; Song, W.; Ai, K.; Lu, L. Functionalizing Metal Nanostructured Film with Graphene Oxide for Ultrasensitive Detection of Aromatic Molecules by Surface-Enhanced Raman Spectroscopy. *ACS Appl. Mater. Inter.* **2011**, 3, 2944-2952.
29. Lu, G.; Li, H.; Liusman, C.; Yin, Z.; Wu, S.; Zhang, H. Surface Enhanced Raman Scattering of Ag or Au Nanoparticle-Decorated Reduced Graphene Oxide for Detection of Aromatic Molecules. *Chem. Sci.* **2011**, *2*, 1817-1821.
30. Zhang, Y.; Liu, S.; Lu, W.; Wang, L.; Tian, J.; Sun, X. In Situ Green Synthesis of Au Nanostructures on Graphene Oxide and Their Application for Catalytic Reduction of 4-Nitrophenol. *Catal. Sci. Technol.* **2011**, *1*, 1142-1144.
31. Wang, J.; Dong, X.; Xu, R.; Li, S.; Chen, P.; Chan-Park, M. B. Template-Free Synthesis of Large Anisotropic Gold Nanostructures on Reduced Graphene Oxide. *Nanoscale* **2012**, *4*, 3055-3059.
32. Hu, C.; Rong, J.; Cui, J.; Yang, Y.; Yang, L.; Wang, Y.; Liu, Y. Fabrication of a Graphene Oxide–Gold Nanorod Hybrid Material by Electrostatic Self-Assembly for Surface-Enhanced Raman Scattering. *Carbon* **2013**, *51*, 255-264.
33. Huang, X.; Li, H.; Li, S.; Wu, S.; Boey, F.; Ma, J.; Zhang, H. Synthesis of Gold Square-Like Plates from Ultrathin Gold Square Sheets: the Evolution of Structure Phase and Shape. *Angew Chem. Int. Ed. Engl.* **2011**, *50*, 12245-12248.
34. Jen Cho, S.; Suri, A.; Mei, X.; Ouyang, J. In Situ Deposition of Gold

Nanostructures with Well-Defined Shapes on Unfunctionalized Reduced Graphene Oxide through Chemical Reduction of a Dry Gold Precursor with Ethylene Glycol Vapor. *RSC Adv.* **2013**, *3*, 1201-1209.

35. Marangoni, V. S., Germano, L. D., Silva, C. C. de Souza, E. A., Maroneze, C. M. Engineering Two-Dimensional Gold Nanostructures Using Graphene Oxide Nanosheets as a Template. *Nanoscale* **2018**, *10*, 13315-13319.
36. Wang, W.; Gu, J.; Hua, W.; Ji, X.; Xi, K. A Novel High Efficiency Composite Catalyst: Single Crystal Triangular Au Nanoplates Supported by Functional Reduced Graphene Oxide. *Chem. Commun.* **2014**, 8889-8891.
37. Geng, G.; Chen, P.; Guan, B.; Liu, Y.; Yang, C.; Wang, N.; Liu, M. Sheetlike Gold Nanostructures/Graphene Oxide Composites via a One-Pot Green Fabrication Protocol and Their Interesting Two-Stage Catalytic Behaviors. *RSC Adv.* **2017**, *7*, 51838-51846.
38. W. Xin, I.M. De Rosa, P. Ye, J. Severino, C. Li, X. Yin, M. S. Goorsky, L. Carlson and J. M. Yang, Graphene Template-Induced Growth of Single-Crystalline Gold Nanobelts with High Structural Tunability, *Nanoscale* **2018**, *10*, 2764-2773.
39. Hong, X.; Tan, C.; Chen, J.; Xu, Z.; Zhang, H. Synthesis, Properties and Applications of One- and Two-Dimensional Gold Nanostructures. *Nano Res.* **2014**, *8*, 40-55.
40. Li, N.; Zhao, P.; Astruc, D. Anisotropic Gold Nanoparticles: Synthesis, Properties, Applications, and Toxicity. *Angew Chem. Int. Ed Engl*. **2014**, *53*, 1756-1789.
41. Wang, J.; Wang, D.; Sobal, N. S.; Giersig, M.; Jiang, M. Mohwald, H. Stepwise Directing of Nanocrystals to Self-Assemble at Water/Oil Interfaces. *Angew Chem. Int. Ed Engl.* **2006**, *45*, 7963-7966.
42. Brust, M.; Walker, M.; Bethell, D.; Schiffrin, D. J.; Whyman, R. Synthesis of Thiol-Derivatised Gold Nanoparticles in a Two-Phase Liquid–Liquid System. *J. Chem. Soc. Chem. Commun.* **1994**, *7*, 801-802.

43. Platt, M.; Dryfe, R. A. W.; Roberts, E. P. L. Structural and Electrochemical Characterisation of Pt and Pd Nanoparticles Electrodeposited at the Liquid/Liquid Interface. *Electrochim. Acta* **2004**, *49*, 3937-3945.
44. Platt, M.; Dryfe, R. A. W. Structural and Electrochemical Characterisation of Pt and Pd Nanoparticles Electrodeposited at the Liquid/Liquid Interface: Part 2. *Phys. Chem. Chem. Phys*. **2005**, *7*, 1807-1814.
45. Rao, C. N. R.; Kulkarni, G. U.; Thomas, P. J.; Agrawal, V. V.; Saravanan, P. Films of Metal Nanocrystals Formed at Aqueous-Organic Interfaces. *J. Phys. Chem. B* **2003**, 107, 7391-7395.
46. Rao, C. N. R.; Kulkarni, G. U.; Agrawal, V. V.; Gautam, U. K.; Ghosh, M.; Tumkurkar, U. Use of the Liquid-Liquid Interface for Generating Ultrathin Nanocrystalline Films of Metals, Chalcogenides, and Oxides. *J. Colloid Interface Sci.* **2005**, *289*, 305-318.
47. Rao C. N. R.; Kalyanikutty, K. P. The Liquid–Liquid Interface as a Medium to Generate Nanocrystalline Films of Inorganic Materials. *Accounts Chem. Res.* **2008**, *4*, 489-499.
48. Sanyal, M. K.; Agrawal, V. V.; Bera, M. K.; Kalyanikutty, K. P.; Daillant, J.; Blot, C.; Kubowicz, S.; Konovalov, O.; Rao, C. N. R. Formation and Ordering of Gold Nanoparticles at the Toluene-Water Interface. *J. Phys. Chem. C*, **2008**, *112*, 1739-1749.
49. Sanyal, M. K. The Use of Grazing Incidence X-Ray Scattering Techniques to Probe Chemical Reactions at the Liquid–Liquid Interface: the Formation and Ordering of Gold Nanoparticles. *J. Mater. Chem.* **2009**, *19*, 1739-1743.
50. Kubowicz, S.; Hartmann, M. A.; Daillant, J.; Sanyal, M. K.; Agrawal, V. V.; Blot, C.; Konovalov, O.; Möhwald, H. Gold Nanoparticles at the Liquid-Liquid Interface: X-Ray Study and Monte Carlo Simulation. *Langmuir* **2009**, *25*, 952-958.
51. Uehara, A.; Booth, S. G.; Chang, S. Y.; Schroeder, S. L.; Imai, T.; Hashimoto, T.; Mosselmans, J. F.; Dryfe, R. A. Electrochemical Insight into the Brust-

Schiffrin Synthesis of Au Nanoparticles. *J. Am. Chem. Soc.* **2015**, *137*, 15135-15144.

52. Peljo, P.; Scanlon, M. D.; Olaya, A. J.; Rivier, L.; Smirnov, E., Girault, H. H. Redox Electrocatalysis of Floating Nanoparticles: Determining Electrocatalytic Properties without the Influence of Solid Supports. *J. Phys. Chem. Lett.* **2017**, *8*, 3564−3575.
53. Smirnov, E.; Peljo, P.; Scanlon, M. D.; Girault, H. H. Interfacial Redox Catalysis on Gold Nanofilms at Soft Interfaces. *ACS Nano* **2015**, *9*, 6565–6575.
54. Peljo, P.; Smirnov, E.; Girault, H. H. Heterogeneous Versus Homogeneous Electron Transfer Reactions at Liquid–Liquid Interfaces: the Wrong Question? *J. Electroanal. Chem.* **2016**, *779*, 187–198.
55. Yao, K.; Lu, W.; Li, X.; Wang, J. Tailoring the Properties of Aqueous–Ionic Liquid Interfaces for Tunable Synthesis and Self-Assembly of ZnS Nanoparticles. *J. Mater. Chem. A* **2014**, 2, 5140-5148.
56. Lu, W.; Yao, K.; Wang, J.; Yuan, J. Ionic Liquids-Water Interfacial Preparation of Triangular Ag Nanoplates and Their Shape-Dependent Antibacterial Activity. *J. Colloid Interf. Sci.* **2015**, *437*, 35-41.
57. Soejima, T.; Kimizuka, N. Ultrathin Gold Nanosheets Formed by Photoreduction at the Ionic Liquid/Water Interface. *Chem. Lett.* **2005**, *34*, 1234-1235.
58. Takagi, S.; Nishi, N.; Sakka, T. Ionic Liquid-In-Water Emulsion-Templated Synthesis of Gold Nanoshells at the Liquid-Liquid Interface between Water and Primary Ammonium-Based Ionic Liquids. *Chem. Lett.* **2019**, *48*, 589-592.
59. Nishi, N.; Kakinami, T.; Sakka, T. Dendritic Nanofibers of Gold Formed by The Electron Transfer at the Interface between Water and a Highly Hydrophobic Ionic Liquid. *Chem. Commun.* **2015**, *51*, 13638-13641.
60. Nishi, N.; Yajima, I.; Amano, K. I.; Sakka, T. Janus-Type

Gold/Polythiophene Composites Formed via Redox Reaction at the Ionic Liquid|Water Interface. *Langmuir* **2018**, *34*, 2441-2447.

61. Zhang, Y.; Nishi, N.; Amano, K.-i.; Sakka, T. One-Dimensional Pt Nanofibers formed by the Redox Reaction at the Ionic Liquid|Water Interface. *Electrochim. Acta* **2018**, *282*, 886-891.
62. Zhang, Y.; Nishi, N.; Sakka, T. Template-Free and Spontaneous Formation of Vertically Aligned Pd Nanofiber Arrays at the Liquid-Liquid Interface between Redox-Active Ionic Liquid and Water. *ACS Appl. Mater. Inter.* **2019**, *11*, 23731-23740.
63. Zhang, Y.; Nishi, N.; Sakka, T. One-Step Fabrication of Au@Pd Core-Shell Bimetallic Nanofibers at the Interface between Water and Redox-Active Ionic Liquid. *Electrochim. Acta* **2019**, *325*, 134919.
64. Nishi, N.; Uruga, T.; Tanida, H.; Kakiuchi, T. Temperature Dependence of Multilayering at the Free Surface of Ionic Liquids Probed by X-Ray Reflectivity Measurements. *Langmuir* **2011**, *27*, 7531-7536.
65. Langmaier, J.; Trojánek, A.; Samec, Z. Electron Transfer Across the Polarized Interface Between Water and a Hydrophobic Redox-Active Ionic Liquid. *Electrochem. Commun.* **2010**, *12*, 1333-1335.
66. Langmaier, J.; Samec, Z. Thermodynamic Aspects of the Electron Transfer Across the Interface between Water and a Hydrophobic Redox-Active Ionic Liquid. *Electrochim. Acta* **2011**, *58*, 606-613.
67. Hummers, W. S.; Offeman, R. E. Preparation of Graphitic Oxide. *J. Am. Chem. Soc.* **1958**, *80*, 1339.
68. Shih, C. J.; Lin, S.; Sharma, R. Strano, M. S.; Blankschtein, D. Understanding the Ph-Dependent Behavior of Graphene Oxide Aqueous Solutions: a Comparative Experimental and Molecular Dynamics Simulation Study. *Langmuir* **2012**, *28*, 235-241.
69. Fang, S.; Chen, T.; Chen, B.; Xiong, Y.; Zhu, Y.; Duan, M. Graphene Oxide at Oil-Water Interfaces: Adsorption, Assembly & Demulsification. *Colloid*

Surface A **2016**, *511*, 47-54.

70. Shao, J. J.; Lv, W.; Yang, Q. H. Self-Assembly of Graphene Oxide at Interfaces. *Adv. Mater.* **2014**, *26*, 5586-5612.
71. Kim, F.; Cote, L. J.; Huang, J. Graphene Oxide: Surface Activity and Two-Dimensional Assembly. *Adv. Mater.* **2010**, *22*, 1954-1958.
72. Kakinami, T.; Nishi, N.; Sakka, T. Preparation of Dendritic Gold Nanofibers Using a Redox Reaction at the Interface between an Ionic Liquid and Water: Correlation between Viscosity and Nanostructure. *Bunsekikagaku*, **2016**, *65*, 157-161.
73. Bard, A. J.; Parsons, R.; Jordan, J. Standard Potentials in Aqueous Solution, *CRC Press* 1985, 287-365.
74. Kong, B. S.; Geng, J.; Jung, H. T. Layer-By-Layer Assembly of Graphene and Gold Nanoparticles By Vacuum Filtration and Spontaneous Reduction of Gold Ions. *Chem. Commun. (Camb)* 2009, 16, 2174-2176.
75. Uehara, A.; Hashimoto, T.; Dryfe, R.A.W. Au electrodeposition at the liquid-liquid Interface: mechanistic aspects, *Electrochim. Acta* **2014**, *118*, 26-32.
76. Emiru, T. F.; Ayele, D. W. Controlled Synthesis, Characterization and Reduction of Graphene Oxide: a Convenient Method for Large Scale Production. *Egyptian Journal of Basic and Applied Sciences* **2017**, *4*, 74-79.
77. Ossonon, B. D.; Bélanger, D. Synthesis and Characterization of Sulfophenyl-Functionalized Reduced Graphene Oxide Sheets. *RSC Adv.* **2017**, *44*, 27224-27234.
78. Millstone, J. E.; Park, S.; Shuford, K. L.; Qin, L.; Schatz, G. C.; Mirkin, C. A. Observation of A Quadrupole Plasmon Mode for a Colloidal Solution of Gold Nanoprisms. *J. Am. Chem. Soc.* **2005**, *127*, 5312-5313.
79. Huang, Y.; Ferhan, A. R.; Gao, Y.; Dandapat, A.; Kim, D. H. High-Yield Synthesis of Triangular Gold Nanoplates with Improved Shape Uniformity, Tunable Edge Length and Thickness. *Nanoscale* **2014**, *6*, 6496-6500.
80. Miranda, A.; Malheiro, E.; Skiba, E.; Quaresma, P.; Carvalho, P. A.; Eaton,

P.; de Castro, B.; Shelnutt, J. A.; Pereira, E. One-Pot Synthesis of Triangular Gold Nanoplates Allowing Broad and Fine Tuning of Edge Length. *Nanoscale* **2010**, *2*, 2209-2216.

81. Wang, H.; Hu, Y. H. Electrolyte-Induced Precipitation of Graphene Oxide in Its Aqueous Solution. *J. Colloid Interf. Sci.* **2013**, *391*, 21-27.
82. Wang, L.; Zhu, Y.; Wang, J. Q.; Liu, F.; Huang, J.; Meng, X.; Xiao, F. S. Two-Dimensional Gold Nanostructures with High Activity for Selective Oxidation of Carbon–Hydrogen Bonds. *Nat. commun.* **2015,** 6, 6957.

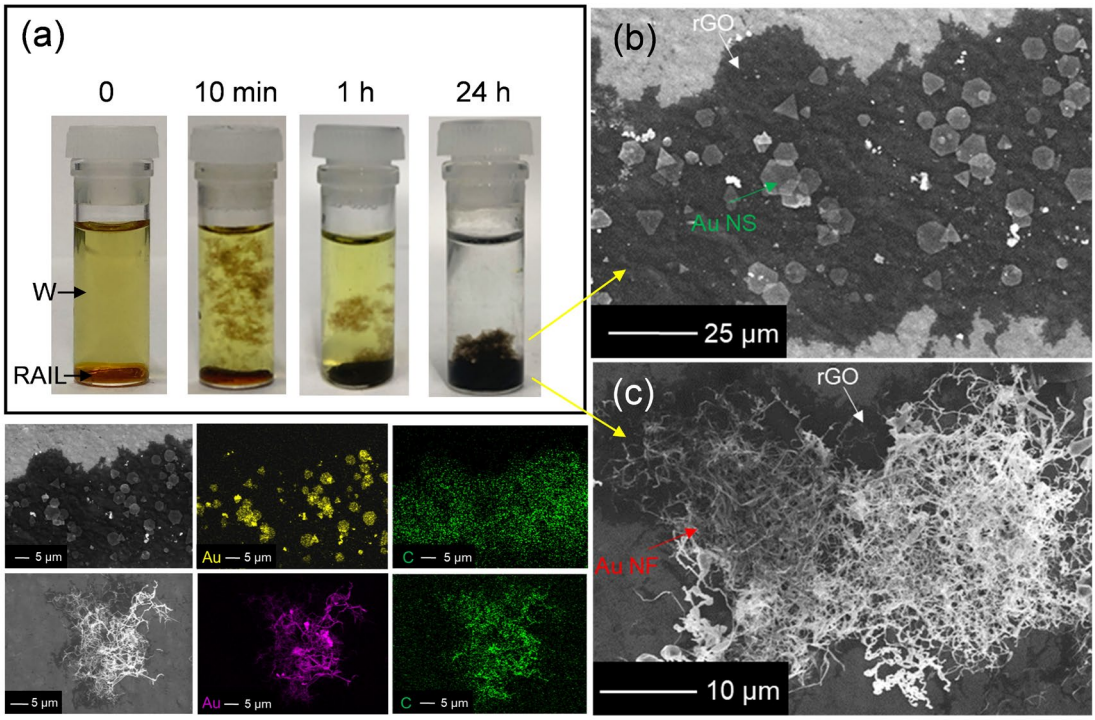

Fig. 1 Photographs of the reaction system before reaction and after 10 min, 1 h, 24 h of reaction (a); SEM images and EDX mappings of Au NS/rGO composites (b, d) and Au NF/rGO composites (c, e).

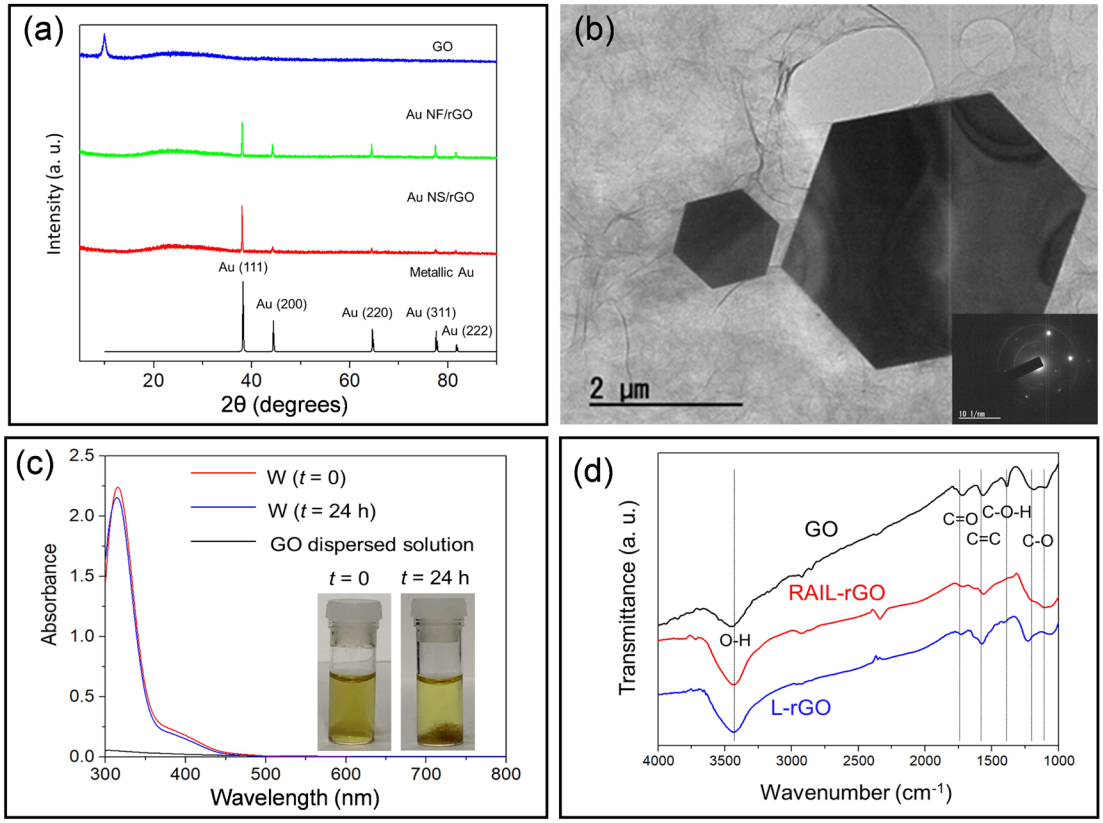

Fig. 2 (a) XRD patterns for the GO obtained by Hummers' method, Au NF/rGO composites, and Au NS/rGO composites; (b) TEM and SAED images (inset) of Au NS/rGO composites; (c) UV-vis spectra for the W (diluted for 15 times) before (red) and after (blue) 24 h reaction as well as the GO dispersed solution diluted as the same concentration that added in W. Inset: Photos of the system before and after 24 h reaction; (d) FTIR spectra for GO, rGO reduced by RAIL (RAIL-rGO), and rGO reduced by L-Asorbic acid (L-rGO) dispersed in KBr pellets.

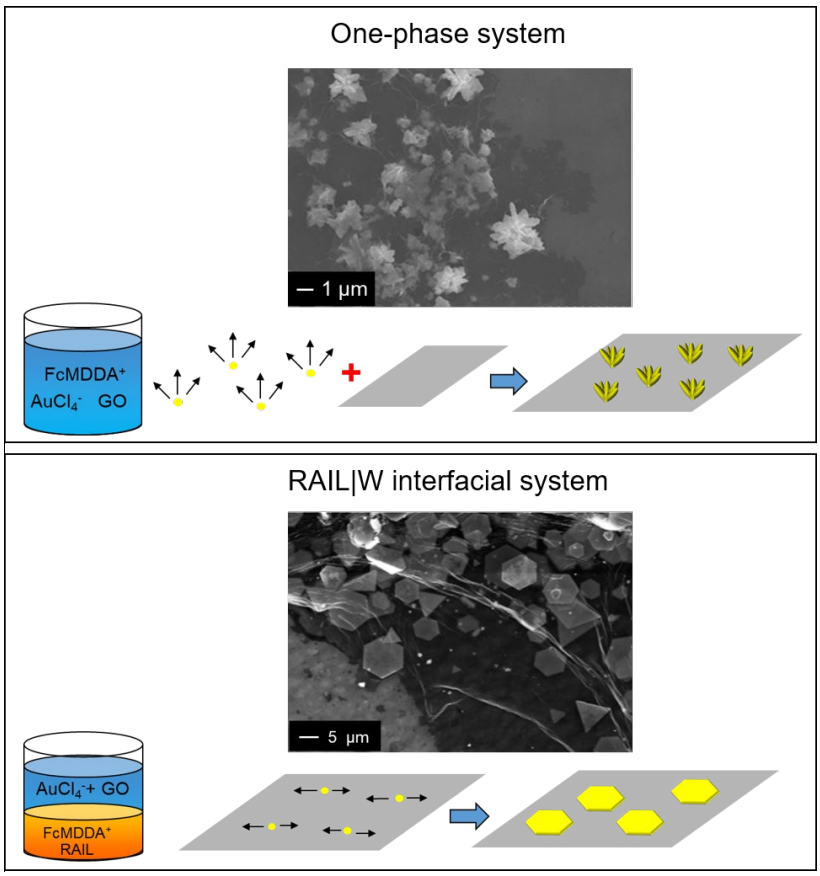

Fig. 3 SEM images and schematics for Au-rGO composites collected from the methanol-diluted one-phase system (see main text for the details, upper), and the bulk W in RAIL|W interfacial system (lower).

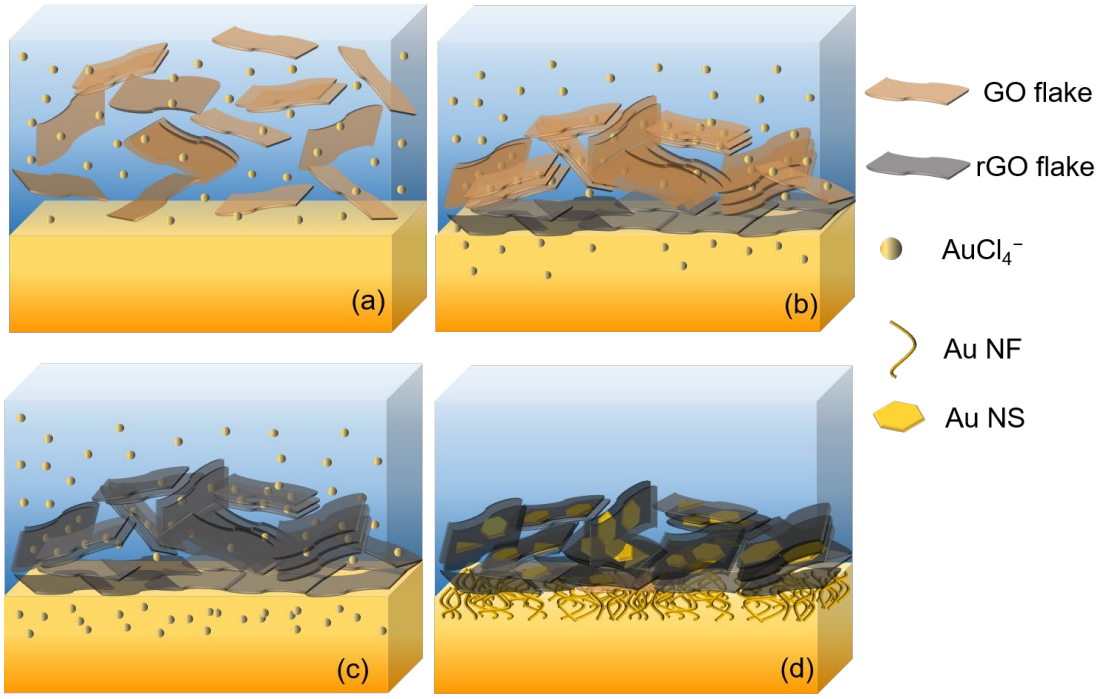

Fig. 4 Schematic for the possible mechanism of the formation of Au NF/rGO and Au NS/rGO composites.

Graphic abstract